White Rose Research Online

eprints@whiterose.ac.uk
https://eprints.whiterose.ac.uk
Universities of Leeds, Sheffield and York

Deposited via The University of Sheffield.

White Rose Research Online URL for this paper:
https://eprints.whiterose.ac.uk/id/eprint/196064/

Version: Accepted Version

**Article:**
Yang, W., Guo, J., Chen, J. et al. (2022) A novel channel inconsistency estimation method for azimuth multichannel SAR based on maximum normalized image sharpness. IEEE Transactions on Geoscience and Remote Sensing, 60. 5237916. ISSN: 0196-2892

https://doi.org/10.1109/tgrs.2022.3219818

© 2022 IEEE. Personal use of this material is permitted. Permission from IEEE must be obtained for all other users, including reprinting/ republishing this material for advertising or promotional purposes, creating new collective works for resale or redistribution to servers or lists, or reuse of any copyrighted components of this work in other works. Reproduced in accordance with the publisher's self-archiving policy.

**Reuse**
Items deposited in White Rose Research Online are protected by copyright, with all rights reserved unless indicated otherwise. They may be downloaded and/or printed for private study, or other acts as permitted by national copyright laws. The publisher or other rights holders may allow further reproduction and re-use of the full text version. This is indicated by the licence information on the White Rose Research Online record for the item.

**Takedown**
If you consider content in White Rose Research Online to be in breach of UK law, please notify us by emailing eprints@whiterose.ac.uk including the URL of the record and the reason for the withdrawal request.

UNIVERSITY OF LEEDS
University of Sheffield
UNIVERSITY of York

# A Novel Channel Inconsistency Estimation Method for Azimuth Multi-channel SAR Based on Maximum Normalized Image Sharpness

Wei Yang, *Member, IEEE*, Jiayi Guo, Jie Chen, *Senior Member, IEEE*, Wei Liu, *Senior Member, IEEE*, Jiadong Deng, Yamin Wang, HongCheng Zeng, *Member, IEEE*

***Abstract*—For azimuth multi-channel synthetic aperture radar (SAR), unavoidable inconsistency errors between channels can degrade SAR image quality severely, leading to possible ghost targets and image defocusing, etc. To address this issue, a novel channel inconsistency estimation method is proposed based on maximum normalized image sharpness. First, channel amplitude and time delay errors are corrected in the coarse compensation step. Then images of each channel are attained by azimuth spectrum recovery and imaging processing. Next, range-variant channel phase errors are estimated via optimizing normalized image sharpness, which reaches the maximum value when the image is focused well or ghost targets are suppressed completely. The Broyden-Fletcher-Goldfarb-Shanno (BFGS) algorithm is employed to get the optimal solution based on the derived gradient of objective function. Finally, the ultimate image is formed through adding up phase compensated images of each channel. By optimizing the focused image quality, the proposed algorithm achieves high estimation accuracy. Simulated data and real multi-channel SAR data are processed to demonstrate the effectiveness of the proposed method.**

***Index Terms*—Azimuth multi-channel synthetic aperture radar (SAR), high-resolution and wide-swath (HRWS), channel inconsistency error estimation, normalized image sharpness.**

## I. Introduction

SYNTHETIC Aperture Radar (SAR) plays significant roles in remote sensing applications. High-resolution and wide-swath (HRWS) has been one of the main goals for SAR system design [1][2]. However, in conventional SAR systems, high resolution in azimuth and wide-swath coverage in range cannot be achieved simultaneously because of their contradicting requirements on pulse repetition frequency (PRF). Azimuth high resolution needs a large Doppler bandwidth which has to be sampled by high PRF, while wide-swath means a long pulse repetition interval corresponding to low PRF. To overcome this system-inherent limitation, the azimuth multi-channel SAR technique was developed [3]-[6] by arranging multiple receiving apertures along the track direction to improve equivalent PRF. Although received signal of one channel is ambiguous, signals of all channels can be combined to obtain Doppler-ambiguity-free spectrum by applying an appropriate reconstruction algorithm [6][7]. The azimuth multi-channel technology has been adopted in several spaceborne SAR systems [8]-[12], and its feasibility and effectiveness have been successfully verified. However, in practice, inconsistency errors between receiving channels are unavoidable, including amplitude errors, time delay errors, channel position errors and phase errors [13], which may introduce azimuth ambiguity components in reconstructed Doppler spectrum and result in ghost targets in the ultimate image, degrading image quality severely. Thus, channel inconsistency error correction is an essential step for multi-channel HRWS SAR image formation[14]-[16]. Channel amplitude errors can be corrected precisely by the channel balancing technique [17], while time delay errors can be estimated via the azimuth cross correlation method with high accuracy [18]. As along-track channel position errors are usually negligible and cross-track position errors can be integrated into channel phase errors [18][19], channel phase error estimation becomes main challenge for channel mismatch correction.

Many approaches have been proposed in recent years to estimate channel phase errors. The simplest method is azimuth time-domain cross-correlation (ATC) [18][20][21], which requires accurate Doppler centroid frequency for estimation [22]. In spite of low computational complexity, the accuracy of the ATC method is relatively low [23][24]. Another estimation method is based on the signal subspace (SSP) theory [13][17][25]-[28], which is more accurate than the ATC method [29]. However, in order to obtain the signal subspace and noise subspace, eigenvalue decomposition of the covariance matrix is required, making the SSP method sensitive to the signal-to-noise ratio (SNR) of raw data. Based on the fact that phase errors could degrade performance of spectrum reconstruction, some methods have been developed by optimizing the Doppler spectrum power distribution [17][30]-[34]. The Doppler spectrum method does not need

This work was supported by the Beijing Natural Science Foundation under Grant No. 4222006. (*Corresponding author: Yamin Wang.*)

Wei Yang, Jiayi Guo, Jie Chen, Jiadong Deng, Yamin Wang and HongCheng Zeng are with the School of Electronic and Information Engineering, Beihang University, Beijing 100191, China (email: yangweigigi@sina.com; jiayiguo@buaa.edu.cn; chenjie@buaa.edu.cn; djdong0725@buaa.edu.cn; wangyamin@buaa.edu.cn; zenghongcheng@buaa.edu.cn).

W. Liu is with the Department of Electronic and Electrical Engineering, University of Sheffield, Sheffield S10 2TN, U.K. (e-mail: w.liu@sheffield.ac.uk)

matrix decomposition, but it is highly dependent on illuminated scenes [32], which works well for uniformly distributed scenes but tends to perform poorly on complex scenes.

The above methods are applied before spectrum reconstruction and imaging processing, and therefore can be called signal-domain methods. Considering the high SNR of focused image, image-domain methods have been developed for a more accurate phase error estimation[35]-[39]. In [35] and [36], the conventional SSP method is extended into the image domain to improve estimation accuracy; however, at least one redundant channel is required for noise subspace decomposition. Since channel phase errors would result in ghost targets in SAR images, range-variant phase errors are estimated by minimizing entropy of the coarsely focused image in [38]. In [39], channel phase errors are obtained through minimizing $L_1$-norm of all ghost targets and real targets in an image. But these methods may not function well when ghost targets are submerged by strong clutter in the image region selected for estimation. In [40], antenna array phase errors are precisely estimated via optimizing contrast of digital beamforming radar image. Nevertheless, the image formation principles of multi-channel SAR and digital beamforming radar are different. Besides, the ghost targets caused by channel phase errors are not considered in [40]. Therefore, it is difficult to directly apply this approach to multi-channel SAR system.

Although existing methods have made remarkable progress, it is still challenging for them to accurately and robustly estimate channel phase errors due to the high variation of SNR and complexity of scenes. To address this challenge, a novel maximum normalized image sharpness (MNIS) approach is proposed to estimate channel phase errors for HRWS multi-channel SAR system. Considering that phase errors would result in ghost targets and defocusing of real targets [38], channel phase error estimation is achieved by optimizing the final SAR image quality. Specifically, the normalized image sharpness (NIS) is adopted as a criterion to measure image quality, which can evaluate the suppression of ghost targets as well as the degree of focus of real targets [41] at the same time. Phase error estimation is modeled as an optimization problem and the objective function is established according to the relationship between channel phase errors and NIS. Since there is no closed-form solution, the Broyden – Fletcher – Goldfarb - Shanno (BFGS)-based quasi-Newton iterative algorithm [43] is employed to obtain the optimized solution based on the derived objective function gradient. In addition, coarsely estimated channel phase errors are set as the initial value of iteration to improve convergence speed. The range-variance of channel phase errors is also considered by dividing images into several blocks along the range direction. The whole channel inconsistency estimation algorithm is described as follows. First, in the coarse channel mismatch compensation step, amplitude and time delay errors are estimated and corrected. Then azimuth spectrum recovery and imaging processing are operated on data of each channel to acquire every channel's focused image. After that, images are divided into several blocks along range. In each block, channel phase errors are assumed to be constant and estimated through the MNIS method. Next, range-variant phase errors are obtained by weighted least squares estimation[45]. Finally, images of all channels are added together after phase error compensation and the ultimate well-focused image without ambiguity is constructed.

Compared with conventional signal-domain methods, the proposed method could achieve higher estimation accuracy since SNR is dramatically improved after imaging processing. In addition, the proposed method does not need a redundant channel, making it more robust than signal subspace methods [35][36]. Furthermore, as the suppression of ghost targets and the degree of focus of real targets are both utilized to evaluate the final SAR image quality, the MNIS method can maintain better performance than other image-domain methods[37]-[39] especially in the case of low SNR or strong clutter. Overall, the main contributions of the proposed method are as follows:

1) A novel method is proposed to estimate channel phase errors accurately and robustly by optimizing normalized SAR image sharpness;

2) The objective function is established based on the relationship between phase errors and NIS. By deriving the objective function gradient, optimal solutions are obtained via BFGS-based quasi-Newton method;

3) Experimental results verify the effectiveness of the proposed method. The results also show that the proposed method outperforms other methods on both simulated and real data.

The reminder of this article is organized as follows. Section II gives the signal model of multi-channel SAR. Section III provides the coarse channel mismatch compensation algorithm. In Section IV, image formation of each channel is realized by azimuth spectrum recovery and imaging processing. In Section V, the MNIS method is proposed to estimate channel phase errors. The range-variant phase error estimation scheme and the flowchart for whole channel inconsistency correction are also presented. In Section VI, the performance of the proposed algorithm is evaluated by simulated and real measured multi-channel SAR data. Conclusions are drawn in Section VII.

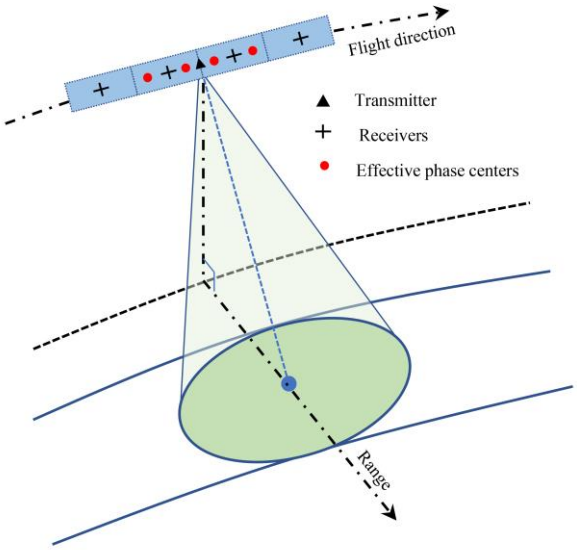


Fig. 1. Operation geometry of a multi-channel SAR system.

## II. Signal Model of Multi-channel SAR

The operation geometry of a multi-channel SAR system is shown in Fig. 1. A single transmitter illuminates an area and *M* receivers arranged uniformly along the along-track direction record signals simultaneously. The effective antenna phase center (EAPC) of signal received by the *m*-th channel is located at the middle of transmitter and corresponding receiver [6]. Assuming $S_0(\tau,t)$ is the ideal reference signal whose phase center is located at the transmitter, the signal of the *m*-th channel can be expressed as [6]:

$$S_m^0(\tau,t)=S_0\left(\tau,t+\frac{d_m}{2v}\right)\quad m=1,.....,M \tag{1}$$

in which $\tau$ and $t$ represent range fast-time and azimuth slow time separately, $d_m$ is displacement between the *m*-th receiver and transmitter. Equation (1) shows that signal received by the *m*-th channel is equivalent to the traditional single-channel signal with a time delay $d_m/2v$.

In practice, channel inconsistency errors are inevitable in multi-channel SAR systems. In addition to amplitude errors, phase errors and time delay errors, antenna position errors caused by installation and satellite attitude error should also be considered. A geometry model for antenna position error is shown in Fig. 2., where the *Y*-axis is in the flight direction of platform with a velocity *v*, the *Z*-axis is away from the center of the earth and the *X*-axis is the cross-azimuth direction. The red line denotes the ideal position trajectory of the antenna and the green line represents the real position trajectory. The nominal position of an EAPC is located at $A_1(0,vt,z_1)$ at time *t*. Assuming antenna position errors along three directions are $\Delta x$, $\Delta y$, and $\Delta z$, the real position of this EAPC at time *t* is $A_2(\Delta x,vt+\Delta y,z_1+\Delta z)$. *P* is the position of a stationary scatter point whose depression angle is $\alpha$.

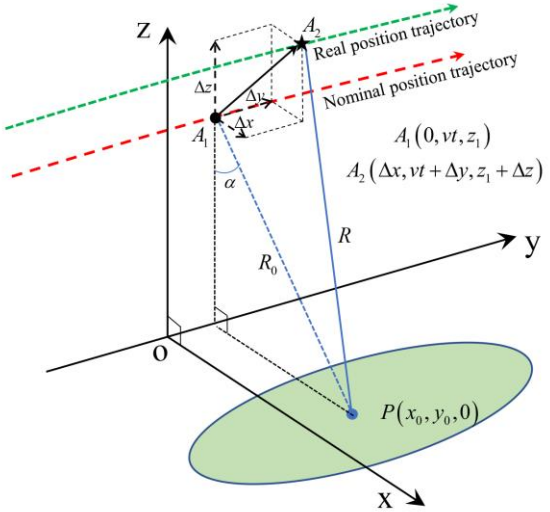


Fig. 2. Geometry model of antenna position error.

The slant range between the ideal EAPC and target *P* at time *t* can be calculated as:

$$R_0(t)=|\vec{A_1P}|=\sqrt{x_0^2+(vt-y_0)^2+z_1^2} \tag{2}$$

Taking antenna position errors into consideration, the real slant range is:

$$\begin{aligned}R(t)&=|\vec{A_2P}|=\sqrt{(x_0-\Delta x)^2+(vt-y_0+\Delta y)^2+(z_1+\Delta z)^2}\\&\approx R_0(t)+\frac{x_0\Delta x+z_1\Delta z-(vt-y_0)\Delta y}{R_0(t)}\end{aligned} \tag{3}$$

For the side-looking mode SAR system, $(vt-y_0)\Delta y \ll R_0(t)$. So (3) can be further written as:

$$\begin{aligned}R(t)&\approx R_0(t)+\frac{x_0\Delta x+z_1\Delta z}{R_0(t)}\\&=R_0(t)+\Delta x\sin\alpha+\Delta z\cos\alpha\end{aligned} \tag{4}$$

Equation (4) indicates that antenna position errors lead to a slant range error varying with depression angle of the target. As antenna position measurement error is usually several millimeters, the range error is also at a level of several millimeters, much smaller than range resolution. Therefore, the influence of range errors on envelopes can be ignored while their effect on phase needs to be considered [26]. For signal of the *m*-th channel, phase error caused by slant range error is:

$$\beta=-4\pi\frac{\Delta x_m\sin\alpha+\Delta z_m\cos\alpha}{\lambda}=-4\pi\frac{\Delta R_m(\alpha)}{\lambda} \tag{5}$$

in which $\Delta x_m$ and $\Delta z_m$ denote antenna position errors of channel *m*. Based on the above analysis, the *m*-th channel signal with channel inconsistency errors can be modeled as:

$$\begin{aligned}S_m^1(\tau,t)&=S_0\left(\tau+\Delta\tau_m,t+\frac{d_m}{2v}\right)A_m\exp(j\phi_m)\\\phi_m&=\varphi_m-4\pi\frac{\Delta R_m(\alpha)}{\lambda}\end{aligned} \tag{6}$$

In (6), $A_m$ and $\Delta\tau_m$ denote amplitude error and time delay error, respectively, and $\phi_m$ denotes phase error, which can be further decomposed into constant phase error $\varphi_m$ and range-variant phase error caused by antenna position error. The estimation and correction of these channel inconsistency errors will be discussed in the following sections.

## III. Coarse Channel Mismatch Compensation

In this section, time delay errors and amplitude errors are estimated and compensated. The first channel is chosen as the reference channel. According to (6), channel phase error may vary with slant range because of antenna position error. However, the coarse channel mismatch estimation and compensation are operated in range-frequency domain, where signals from different slant ranges share the same bandwidth. After performing Fast Fourier Transform (FFT) along range direction, channel phase error is a constant value. Thus, the range-variance of phase error is temporarily ignored in this section. Amplitude errors between channels can be estimated by the channel balancing technique [17]. After amplitude error correction, the *m*-th channel signal in range frequency domain can be expressed as:

$$S_m^2(f_\tau,t)=S_0\left(f_\tau,t+\frac{d_m}{2v}\right)\exp(j\phi_m)\exp(j2\pi f_\tau\Delta\tau_m) \tag{7}$$

where $f_\tau$ denotes range frequency. The last linear phase term in (7) is introduced by time delay error, which can be estimated by the azimuth cross correlation method [18]. First, the phase information is extracted from the cross correlation between two

adjacent channel signals:

$$\begin{aligned} Ph_m(f_\tau) &= \arg\left(E_\eta\left\{S_m^{2*}(f_\tau,t)\cdot S_{m+1}^2(f_\tau,t)\right\}\right) \\ &= 2\pi f_\tau(\Delta\tau_{m+1}-\Delta\tau_m)+\phi_m-\phi_{m-1}+2\pi f_{dc}\frac{\Delta d}{2v} \end{aligned} \tag{8}$$

in which $E_\eta(\cdot)$ denotes statistical expectation along azimuth time, $(\cdot)^*$ denotes the complex conjugate operation, $\arg(\cdot)$ denotes the phase extraction operation, $f_{dc}$ denotes the Doppler centroid frequency and $\Delta d$ is the displacement between two adjacent channels. Then, the relative time delay error between the *m*-th channel and *m+1*-th channel is obtained by [18]

$$\Delta\tau_{m+1}-\Delta\tau_m=\frac{1}{2\pi}\frac{dPh_m(f_\tau)}{df_\tau} \tag{9}$$

After circle accumulation, time delay error between the *m*-th channel and reference channel can be corrected via multiplying a linear term:

$$S_m^3(f_\tau,t)=S_m^2(f_\tau,t)\cdot\exp(-j2\pi f_\tau\Delta\tau_m) \tag{10}$$

As Doppler bandwidth is much larger than the pulse repetition frequency, Doppler spectrum aliasing occurs in each channel. Considering Doppler spectrum ambiguity, signal of the *m*-th channel in azimuth frequency domain after amplitude and time delay error calibration can be expressed as:

$$S_m^3(\tau,f)=\exp(j\phi_m)\sum_{l=-L}^{L}S_0(\tau,f+l\cdot\mathrm{PRF})\exp\left\{j2\pi(f+l\cdot\mathrm{PRF})\frac{d_m}{2v}\right\} \tag{11}$$

where PRF indicates the real system PRF, *f* denotes azimuth frequency, $-\mathrm{PRF}/2\le f\le\mathrm{PRF}/2$, and *2L+1* is the Doppler ambiguity number (for simplicity, we consider an odd number).

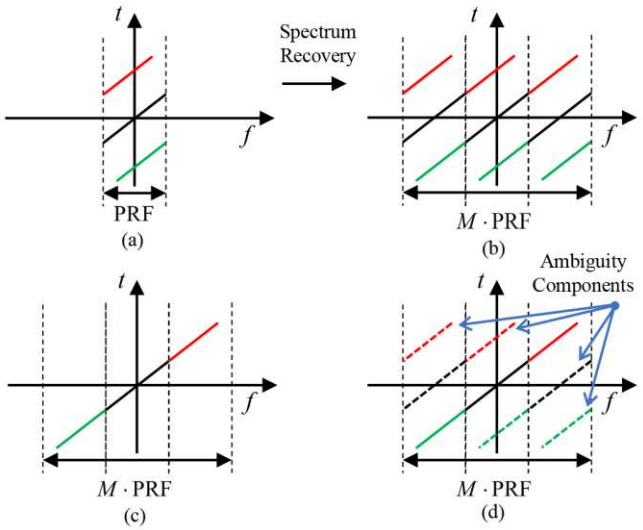


Fig. 3. Azimuth time-frequency domain diagram of a point-like target for multi-channel SAR in strip-map mode. *t* and *f* denote azimuth time and azimuth frequency separately. (a) Signal of one channel with ambiguity. (b) Recovered signal of one channel with ambiguity. (c) Unambiguous reconstructed signal without channel errors. (d) Ambiguous reconstructed signal with channel errors.

## IV. Image Formation of Each Channel

In order to realize wide range swath, the PRF in an azimuth multi-channel SAR system is below the Nyquist sampling rate. Theoretically, PRF should be chosen carefully to obtain a uniform sampling of received signal. However, such a rigid condition may be in conflict with other system design requirements. In practice, the received signals are quite likely to be non-uniformly sampled. Consequently, azimuth spectrum reconstruction must be implemented on signals of all channels to recover the unambiguous Doppler spectrum [6]. Conventionally, imaging processing is adopted after Doppler spectrum reconstruction to obtain the final image. However, the reconstructed spectrum can be modeled as linear superposition of recovered spectrums of each channel. Therefore, it is possible to get images of every channel firstly and then generate the ultimate image by linear superposition. In this section, image formation of each channel is realized by azimuth spectrum recovery and imaging processing.

### A. Azimuth Spectrum Recovery

Data acquisition of each channel can be considered as a linear system with a low-pass filter. Let $\mathbf{H}_m(f)$ be the transfer function of channel *m*. Signals of *M* channels in azimuth frequency domain with phase errors can be modeled in a matrix form:

$$\mathbf{S}_M=\mathbf{EHS}_0 \tag{12}$$

with

$$\mathbf{S}_M=\left[S_1^3(f)\quad S_1^3(f)\quad\cdots\quad S_M^3(f)\right]^T \tag{13}$$

$$\mathbf{S}_0=\left[S_{01}\quad S_{02}\quad\cdots\quad S_{0M}\right]^T \tag{14}$$

$$\mathbf{E}=\mathrm{diag}\left[\exp(j\phi_1)\quad\exp(j\phi_2)\quad\cdots\quad\exp(j\phi_M)\right] \tag{15}$$

$$\mathbf{H}=\left[\mathbf{H}_1(f)\quad\mathbf{H}_2(f)\quad\cdots\quad\mathbf{H}_M(f)\right]^T \tag{16}$$

$$\mathbf{H}_m(f)=\left[\mathrm{e}^{j2\pi f\frac{d_m}{2v}}\quad\mathrm{e}^{j2\pi(f+\mathrm{PRF})\frac{d_m}{2v}}\quad\cdots\quad\mathrm{e}^{j2\pi(f+(M-1)\mathrm{PRF})\frac{d_m}{2v}}\right] \tag{17}$$

in which $S_m^3(f)$ denotes the *m*-th channel signal in azimuth frequency domain, $S_{0m}(f)$ denotes part of the ideal unambiguous spectrum $S_0(f+(m-1)\cdot\mathrm{PRF})$, $\mathbf{H}$ is the transfer function, $[]^T$ denotes the transpose operator and diag{ } denotes a diagonal matrix. $\mathbf{H}$ can be further decomposed as:

$$\mathbf{H}=\mathbf{QP} \tag{18}$$

with

$$\mathbf{Q}=\mathrm{diag}\left[\mathrm{e}^{j2\pi f\frac{d_1}{2v}}\quad\mathrm{e}^{j2\pi f\frac{d_2}{2v}}\quad\cdots\quad\mathrm{e}^{j2\pi f\frac{d_M}{2v}}\right] \tag{19}$$

$$\mathbf{P}=\begin{bmatrix} 1 & \mathrm{e}^{j2\pi\mathrm{PRF}\frac{d_1}{2v}} & \cdots & \mathrm{e}^{j2\pi(M-1)\mathrm{PRF}\frac{d_1}{2v}} \\ \cdots & \cdots & \cdots & \cdots \\ \cdots & \cdots & \cdots & \cdots \\ 1 & \mathrm{e}^{j2\pi\mathrm{PRF}\frac{d_M}{2v}} & \cdots & \mathrm{e}^{j2\pi(M-1)\mathrm{PRF}\frac{d_M}{2v}} \end{bmatrix} \tag{20}$$

where $\mathbf{P}$ is a constant matrix independent of Doppler frequency *f*, and $\mathbf{Q}$ is a diagonal matrix. The spectrum reconstruction process can be realized by multiplying with the inverse matrix $(\mathbf{EH})^{-1}$ [6]:

$$\mathbf{S}_0=\mathbf{H}^{-1}\mathbf{E}^{-1}\mathbf{S}_M=\mathbf{P}^{-1}\mathbf{Q}^{-1}\mathbf{E}^{-1}\mathbf{S}_M=\mathbf{GQ}^{-1}\mathbf{E}^{-1}\mathbf{S}_M \tag{21}$$

in which $\mathbf{G}=\mathbf{P}^{-1}$ is also a constant matrix independent of Doppler frequency, and $\mathbf{Q}^{-1}$ and $\mathbf{E}^{-1}$ can be easily acquired by:

$$\mathbf{Q}^{-1}=\mathrm{diag}\left[\mathrm{e}^{-j2\pi f\frac{d_1}{2v}}\quad\mathrm{e}^{-j2\pi f\frac{d_2}{2v}}\quad\cdots\quad\mathrm{e}^{-j2\pi f\frac{d_M}{2v}}\right] \tag{22}$$

$$\mathbf{E}^{-1}=\mathrm{diag}\left[\exp(-j\phi_1)\quad\exp(-j\phi_2)\quad\cdots\quad\exp(-j\phi_M)\right] \tag{23}$$

In order to emphasize the relationship between channel phase errors and reconstructed spectrum, (21) can be re-arranged as [37]:

$$\begin{aligned}\mathbf{S}_0 &= \sum_{m=1}^{M}\exp(-j\phi_m)S_m^3(f)\cdot \mathrm{e}^{-j2\pi f\frac{d_m}{2v}}\cdot\mathbf{g}_m \\ &= \sum_{m=1}^{M}\exp(-j\phi_m)\mathbf{S}_{m_r}\end{aligned} \tag{24}$$

where $\mathbf{g}_k$ denotes the $k$-th column of $\mathbf{G}$, $\mathbf{S}_{m_r}$ denotes recovered spectrum components of the $m$-th channel, $\mathbf{S}_0$ denotes the unambiguous components. The full unambiguous Doppler spectrum $S_0^{'}(\tau, f_a)$ can be reconstructed by arranging the extracted components from (24):

$$S_0^{'}(\tau, f_a) = \sum_{m=1}^{M}\exp(-j\phi_m)S_{m_r}(\tau, f_a) \tag{25}$$

in which $f_a$ denotes the azimuth frequency after spectrum recovery, $-M\cdot \mathrm{PRF}/2 \le f_a \le M\cdot \mathrm{PRF}/2$ . $S_{m_r}(\tau, f_a)$ is the recovered spectrum of the $m$-th channel. Although its spectrum range is extended to $M\cdot \mathrm{PRF}$, the spectrum is still aliased. The full unambiguous Doppler spectrum can be obtained by adding all recovered spectrums after phase error correction, during which the ambiguous components are removed. If phase errors are not compensated accurately, the reconstructed spectrum will still have ambiguity, as shown in Fig. 3.

### B. Imaging Processing

Imaging algorithms can be implemented on the reconstructed spectrum to form the final focused SAR image. The Chirp Scaling algorithm (CSA) is utilized in this paper to complete image focusing [44]. Let $\Theta(\cdot)$ denotes the imaging operator. The image formation process can be expressed as:

$$\Theta\left(S_0^{'}(\tau, f_a)\right) = \Theta\left(\sum_{m=1}^{M}\exp(-j\phi_m)S_{m_r}(\tau, f_a)\right) \tag{26}$$

CSA can be considered as a linear operator. Reconstructed Doppler spectrum is also linear superposition of recovered spectrums from each channel. Then the final image is:

$$\begin{aligned}I(\tau,t) &= \Theta\left(\sum_{m=1}^{M}\exp(-j\phi_m)S_{m_r}(\tau, f_a)\right) \\ &= \sum_{m=1}^{M}\exp(-j\phi_m)\Theta\left(S_{m_r}(\tau, f_a)\right) = \sum_{m=1}^{M}\exp(-j\phi_m)I_m(\tau,t)\end{aligned} \tag{27}$$

where $I(\tau,t)$ is focused image from $S_0(\tau, f_a)$ and $I_m(\tau,t)$ is imaging result of the $m$-th channel which is obtained by performing imaging processing on $S_{m_r}(\tau, f_a)$ . In discrete domain, (27) can be written as:

$$I(n,k) = \sum_{m=1}^{M}\exp(-j\phi_m)I_m(n,k) \quad n=1,2,...,N \quad k=1,2,...,K \tag{28}$$

where $I(n,k)$ is the discrete form of $I(\tau,t)$ and $I_m(n,k)$ is that of $I_m(\tau,t)$, $n$ is an index to azimuth, and $k$ is an index to range. Equation (28) shows that the final imaging result is equivalent to the weighted sum of imaging results of all channels. This directly establishes the relationship between channel phase errors and image data. Although the image from one channel contains ambiguous components, a well-focused and well-suppressed image can be acquired by compensating accurate phase errors and summing up all images. Fig. 4. shows the process of image formation for each channel, and Fig. 5. illustrates construction of the final well-focused image via superposition. Note that (27) is derived based on the fact that CSA is a linear operator. In addition to CSA, other linear imaging algorithms can also be exploited to achieve image formation for each channel.

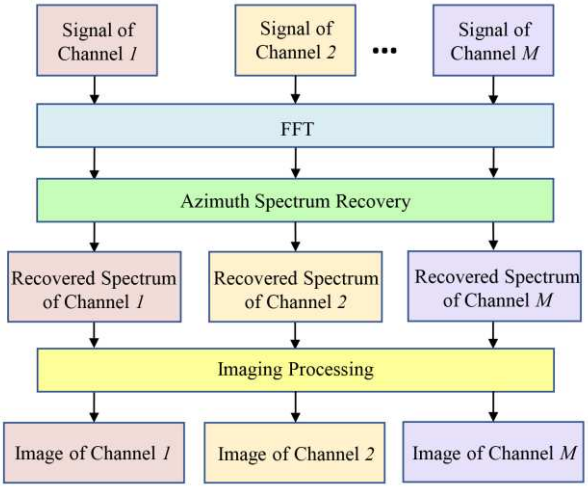


Fig. 4. Image formation of each channel.

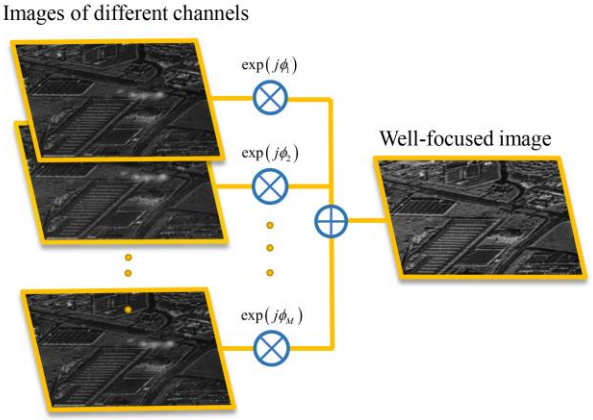


Fig. 5. Construction of the final well-focused image.

## V. Image Domain Channel Phase Error Estimation

In this section, a novel image domain channel phase error estimation algorithm is presented by maximizing the normalized sharpness of the final image, which is called MNIS method. The range-variant channel phase error correction scheme is also discussed and the whole channel calibration diagram is provided.

### A. Normalized Image Sharpness

The final well-suppressed image can be obtained by adding up all images from different channels when phase errors are accurately corrected; otherwise, the image quality will degrade due to phase mismatch. The influence of channel phase error on image mainly includes two aspects: appearance of ghost targets on both sides of real targets along azimuth direction (as shown in Fig. 6. (a)) and defocusing of real targets (as shown in Fig. 6. (b)). The reason is that with existence of phase errors, the ambiguous components are not suppressed completely and the

full Doppler spectrum cannot be reconstructed well. The simulation parameters of Fig. 6 are shown in Table I. Added phase errors for the three channels are $0^{\circ}$, $20^{\circ}$, $15^{\circ}$ separately.

TABLE I
SIMULATION PARAMETERS FOR A THREE-CHANNEL SAR SYSTEM

| Parameter | Value |
|---|---|
| Carrier frequency | 9.6GHz |
| Platform velocity | 6811m/s |
| Slant range | 1050Km |
| Channel numbers | 3 |
| Displacement between adjacent channels | 4m |
| Doppler bandwidth | 2200Hz |
| Pulse repetition frequency | 860Hz |
| Signal bandwidth | 45MHz |

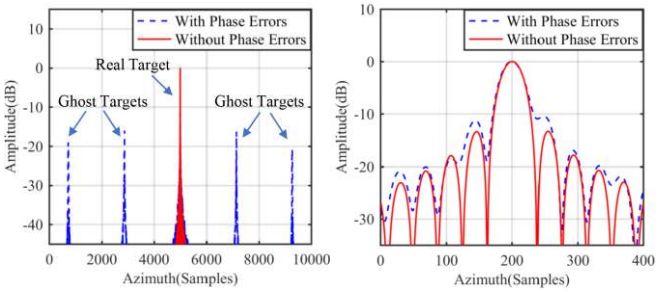


(a) (b)

Fig. 6. Interpolated azimuth profile of a point target with and without phase errors for a SAR system with three channels. (a) Azimuth profile of real target and ghost targets. (b) Enlarged real target in (a).

Since the final image quality is closely related with the accuracy of compensated phase errors, phase error estimation can be achieved by optimizing image quality. There are many criteria to assess SAR image quality [40]-[42]. Image sharpness is an effective function to evaluate the degree of focus in a SAR image, which can be expressed as [41]:

$$\mathrm{Sh}=\sum_{n=1}^{N}\sum_{k=1}^{K}\left[-\ln\left(\left|I(n,k)\right|^{2}+b\right)\right] \tag{29}$$

where $b$ denotes image average intensity. It is often exploited in autofocusing algorithms which realize SAR image refocusing by phase error compensation in the frequency domain. According to the Parseval theorem, image energy is a constant value during the autofocusing process. However, (28) indicates that the multi-channel SAR image energy may change with channel phase errors. Fig. 7. shows the relationship between image average energy and compensated phase errors for a three channel SAR system. The first channel is set as the reference channel and the phase errors of another two channels are assumed to be zero. Fig. 7. indicates that the energy of a multi-channel SAR image varies with compensated phase errors. Besides, the image energy neither reaches the maximum nor the minimum value when the channel phase errors are completely compensated.

In order to ensure that images with different phase errors have the same energy, a normalization operation is performed, making it possible to compare sharpness of different images under the same condition. The normalized image sharpness is:

$$\mathrm{Sh}_{0}=\sum_{n=1}^{N}\sum_{k=1}^{K}\left[-\ln\left(\left|T(n,k)\right|^{2}+b\right)\right] \tag{30}$$

$$T(n,k)=I(n,k)\sqrt{\frac{NK}{\sum_{n=1}^{N}\sum_{k=1}^{K}\left|I(n,k)\right|^{2}}} \tag{31}$$

in which $T(n,k)$ is the normalized image. The main difference between (29) and (30) is that the image average energy is normalized to a constant value:

$$b=\frac{1}{NK}\sum_{n=1}^{N}\sum_{k=1}^{K}\left(T(n,k)\right)^{2}=1 \tag{32}$$

Since channel phase errors lead to image defocusing, the targets' NIS reaches maximum value when phase errors are compensated correctly. In addition to defocusing, channel phase errors also bring ghost targets in SAR image. For regions containing both real targets and ghost targets, NIS will also reach the maximum value when all ghost targets are suppressed, which is analyzed in detail in Appendix A.

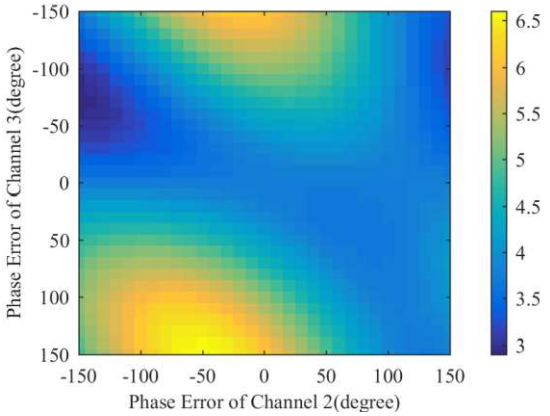


Fig. 7. Image energy variation with phase errors for a three-channel SAR system.

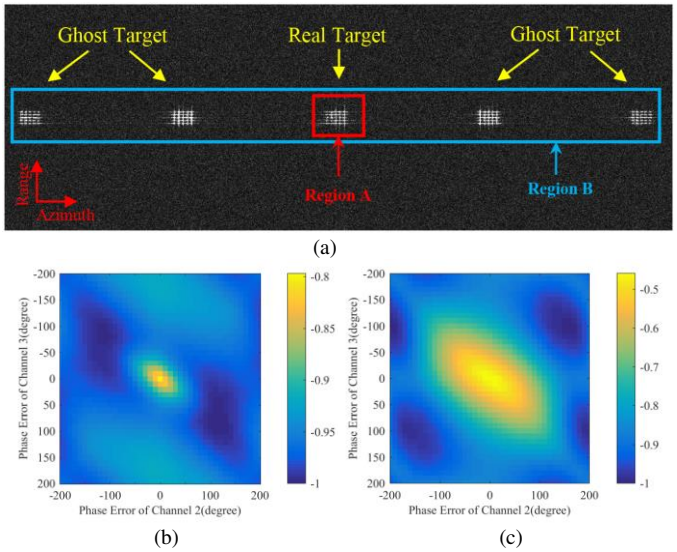


(a) (b) (c)

Fig. 8. Normalized image sharpness for a three-channel SAR system with different phase errors. (a) Imaging result of one channel. (b) Relationship between channel phase errors and NIS for Region B in (a), which contains both real targets and ghost targets. (c) Relationship between channel phase errors and NIS for Region A in (a), which contains real targets only.

Fig. 8. (a) demonstrates a simulated imaging result for a SAR system with three channels. The simulation parameters are shown in Table 1. Positions of real targets and ghost targets are marked by yellow arrows. The first channel is set as the

reference channel. Fig. 8. (b) shows relationship between phase errors of another two channels and NIS for Region B, which contains both real targets and ghost targets, while Fig. 8. (c) shows NIS for Region A, which contains real targets only. Because phase errors are not added during simulation, NIS for both region A and Region B reaches maximum value when phase errors are zero, validating the effectiveness of NIS as a criterion for image quality of multi-channel SAR.

### *B. Phase Error Estimation Based on MNIS via BFGS*

Based on above analysis, phase error estimation can be transformed into an optimization problem, whose objective is to look for a series of phases $\boldsymbol{\theta}=[\theta_1,\theta_2,.....,\theta_M]^T$ to maximize normalized image sharpness. The optimization model is given by

$$\boldsymbol{\theta}=\arg\max_{\hat{\boldsymbol{\theta}}} J(\boldsymbol{\theta}) \tag{33}$$

where $\theta_m$ is the estimation of $-\phi_m$. Combining (28) and (30), the optimization function $J(\boldsymbol{\theta})$ is expressed as follows:

$$J(\boldsymbol{\theta})=\sum_{n=1}^{N}\sum_{k=1}^{K}\left[-\ln\left(\frac{NK\left|\sum_{m=1}^{M}\exp(j\theta_m)I_m(n,k)\right|^2}{\sum_{n=1}^{N}\sum_{k=1}^{K}\left|\sum_{m=1}^{M}\exp(j\theta_m)I_m(n,k)\right|^2}+1\right)\right] \tag{34}$$

Many algorithms are available to tackle such an unconstrained maximization problem. In [37], a monotonic iterative algorithm based on coordinate descent is utilized to minimize image entropy, in which one phase error is updated at a time with all others fixed. Due to the coupling between different channel phase errors, this method needs a lot of iterations to get an accurate value. In [31], Newton's method is adopted to optimize the Doppler spectrum distribution, in which the first-order and second-order derivatives of the objective function are calculated to obtain the searching direction of phase error vector. However, Hessian matrix of (34) is very complex to calculate and it is difficult to ensure positive definiteness when the estimated value deviates greatly from the real value, making Newton's method invalid. In this paper, the BFGS algorithm [43], a quasi-Newton iteration method, is adopted to obtain the optimal solution in (33). Instead of using the second-order derivative to build Hessian matrix, only the gradient operation is needed to establish an approximate Hessian matrix.

The gradient of objective function is:

$$\nabla(\mathbf{J})=\left[\frac{\partial J(\boldsymbol{\theta})}{\theta_1},\frac{\partial J(\boldsymbol{\theta})}{\theta_2},...,\frac{\partial J(\boldsymbol{\theta})}{\theta_M}\right]^T \tag{35}$$

The detailed procedure for gradient derivation can be found in Appendix B. Let $\boldsymbol{\theta}_0$ be the initial phase error vector, $\boldsymbol{\theta}_i$ be the phase error of the $i$-th iteration, and $\mathbf{D}_0=\mathbf{I}_{M\times M}$. Matrix $\mathbf{I}$ is the identity matrix. The searching direction is updated as:

$$\mathbf{d}_i=-\mathbf{D}_i\cdot\nabla\mathbf{J}_i \tag{36}$$

The $i$+1-th phase errors can be expressed as:

$$\boldsymbol{\theta}_{i+1}=\boldsymbol{\theta}_i+\lambda_i\cdot\mathbf{d}_i \tag{37}$$

where $\lambda_i$ is the searching step which can be estimated by:

$$\lambda_i=\arg\max_{\lambda_i}\mathbf{J}(\boldsymbol{\theta}_i+\lambda_i\mathbf{d}_i) \tag{38}$$

The Hessian matrix $\mathbf{D}_i$ is updated as [43]:

$$\mathbf{D}_{i+1}=\left(\mathbf{I}-\frac{\mathbf{s}_i\mathbf{y}_i^T}{\mathbf{y}_i^T\mathbf{s}_i}\right)\mathbf{D}_i\left(\mathbf{I}-\frac{\mathbf{y}_i\mathbf{s}_i^T}{\mathbf{y}_i^T\mathbf{s}_i}\right)+\frac{\mathbf{s}_i\mathbf{s}_i^T}{\mathbf{y}_i^T\mathbf{s}_i} \tag{39}$$

in which $\mathbf{s}_i=\lambda_i\cdot\mathbf{d}_i$ and $\mathbf{y}_i=\nabla\mathbf{J}_{i+1}-\nabla\mathbf{J}_i$. The iteration termination condition is $\|\nabla\mathbf{J}_{i+1}\|\le\varepsilon$, in which $\varepsilon$ denotes the required threshold for accuracy. The smaller the value of $\varepsilon$ is, the more accurate the estimation is, and more iterations are then required with a higher computational complexity. When the termination condition is satisfied, the estimation of channel phase error vector $\boldsymbol{\theta}=[\theta_1,\theta_2,.....,\theta_M]^T$ is accomplished. In order to reduce the number of iterations, coarsely-estimated channel phase errors are set as the initial value, which can be obtained via the azimuth cross correlation method presented in Section III. Detailed steps for the MNIS method are summarized as follows:

*Step 1*: Initialize the phase error vector.

*Step 2*: Calculate the search direction via (39).

*Step 3*: Select step size via line search according to (38).

*Step 4*: Update the phase error vector.

*Step 5*: If the termination condition is satisfied, stop; otherwise, return to Step 2.

### *C. Range-variant Phase Error Compensation Scheme*

Due to the existence of antenna position error, channel phase errors change slightly with targets' depression angle. After imaging, signals of different scatter points are focused in corresponding range bins, making it possible to conduct range-variant phase error correction more precisely. According to the relationship between depression angle and slant range, the channel phase error in (6) can be written as:

$$\begin{aligned}\phi_m&=\varphi_m-4\pi\frac{\Delta R_m(\alpha)}{\lambda}=\varphi_m-4\pi\frac{\Delta x_m\sin\alpha+\Delta z_m\cos\alpha}{\lambda}\\&=\varphi_m-\frac{4\pi}{\lambda}\left(\frac{\Delta x_m\sqrt{r^2-h^2}}{r}+\frac{\Delta z_m h}{r}\right)\end{aligned} \tag{40}$$

where $h$ denotes orbit altitude, $r$ denotes slant range. Let $r_s$ be the reference slant range of the middle range bin and $\Delta r$ be $r-r_s$. Then we have $1/r\approx 1/r_s-\Delta r/r_s^2$ and (40) is simplified as [37]:

$$\phi_m\approx\varphi_m-\frac{4\pi}{\lambda}\left(\Delta x_m-\Delta x_m\frac{h^2}{2r_s^2}+\Delta z_m\frac{h}{r_s}\right)-\frac{4\pi}{\lambda}\left(\frac{h^2}{r_s^3}\Delta x_m-\frac{h}{r_s^2}\Delta z_m\right)\Delta r \tag{41}$$

In (41), the channel phase error is decomposed into two constant components and one linear component corresponding to slant range. The slope is determined by antenna position errors.

Although channel phase errors show range-dependence along the whole range swath, it is considered to be approximately constant within several range bins. In order to estimate range-variant phase errors, the data are processed as follows. Firstly, images of each channel are divided into $G$ blocks along range. Then, the proposed MNIS algorithm is performed on each range block. Note that range bins with higher SNR value should contribute more to range-variant phase error estimation compared with range bins with lower SNR value. According to the linear relationship between phase error and slant range, the range-variant phase errors can be acquired by weighted least squares estimation[45]. Let $y_{gm}$ be the estimated phase error of the $g$-th block and $m$-th channel.

The phase error matrix can be written as $\mathbf{Y}_{G\times M}$, in which $y_{gm}$ represents the element in the $n$-th row and the $m$-th column of the matrix. Let $r_g$ be the center slant range of the $g$-th block. The slant range matrix is expressed as:

$$\mathbf{X}=\begin{bmatrix}1 & 1 & \cdots & 1\\ r_1 & r_2 & \cdots & r_G\end{bmatrix}^T \tag{42}$$

The coefficient matrix to be estimated is defined as:

$$\mathbf{A}=\begin{bmatrix}a_1^0 & a_2^0 & \cdots & a_M^0\\ a_1^1 & a_2^1 & & a_M^1\end{bmatrix}_{2\times M} \tag{43}$$

in which $a_m^0$ and $a_m^1$ represent constant term and the first order coefficient of the $m$-th channel phase error. The weight matrix is defined as:

$$\mathbf{W}=\mathrm{diag}\begin{bmatrix}w_1 & w_2 & \ldots & w_G\end{bmatrix}_{G\times G} \tag{44}$$

in which $w_g$ is the average energy of the $g$-th block. The weighted least squares estimation for the coefficient matrix can be expressed as [45]:

$$\mathbf{A}=\left(\mathbf{X}^T\mathbf{W}\mathbf{X}\right)^{-1}\mathbf{X}^T\mathbf{W}\mathbf{Y} \tag{45}$$

Then the range-variant phase error of the $m$-th channel can be obtained by:

$$\theta_m(r)=a_m^0+a_m^1\cdot r \tag{46}$$

Fig. 9. illustrates a diagram for the range-variant phase error estimation scheme. In addition, the size of regions selected for estimation determines the computational load, with a larger region resulting in a higher computational load. Thus, it is possible to accelerate calculation by reducing data for estimation. After focused images of each channel have been obtained, we can select regions with relatively high SNR to complete phase error estimation. In order to make sure sufficient range-variant phase error information can be provided, the selected regions should be distributed over a wide extent along range direction.

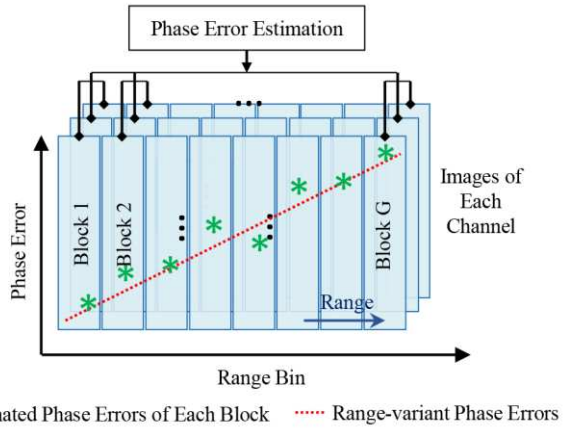


Fig. 9. Range-variant Phase Error Estimation.

### D. *Flowchart of the Proposed Method*

The flowchart of the proposed channel inconsistency error estimation and correction algorithm is shown in Fig. 10. First, time delay errors and amplitude errors are estimated and corrected by the azimuth cross correlation approach. Then, azimuth spectrum recovery and imaging processing are conducted to complete image formation of each channel. Next, images are divided into several blocks along range. In each block, the MNIS method is performed and range-variant phase errors are obtained via adopting weighted least squares estimation. After phase inconsistency compensation, the final well-focused and suppressed image can be acquired through adding up images of all channels. It should be noted that iterations are required for the proposed MNIS algorithm. Taking coarsely estimated phase errors as initial values can increase convergence speed.

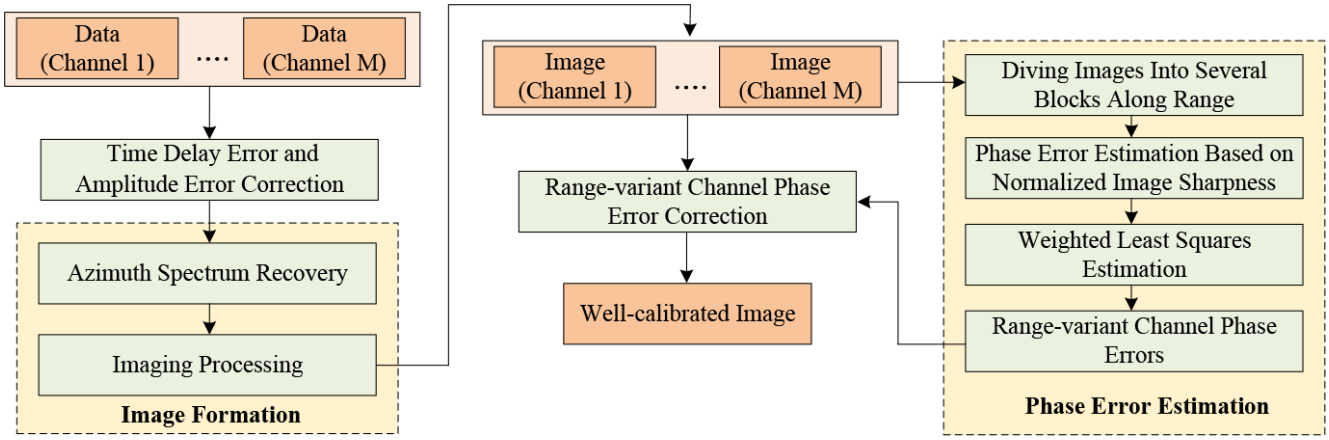


Fig. 10. Flowchart of the proposed channel inconsistency correction algorithm.

## VI. Experimental Results

In this section, both simulated data and real measured data are processed to evaluate the performance of the proposed MNIS method in comparison with another two image-domain methods. In simulated data processing, phase error estimation accuracy is analyzed under different SNR values. In real data processing, the effectiveness of the MNIS method and the range-variant phase error estimation scheme is demonstrated via processing real measured airborne multi-channel SAR data.

### A. *Experiment for Simulated SAR Data*

Simulated multi-channel spaceborne SAR data in strip-map mode is generated. The simulation parameters are listed in Table II. The Doppler ambiguity number is about 3.5 and the channel number is 5. For each SNR, 50 Monte Carlo experiments are carried out. Phase errors of each channel are set as random variables which vary form $-\pi$ to $\pi$. The proposed MNIS method is compared with the image-domain subspace

(ISP) method [36], the local maximum-likelihood weighted minimum entropy (LML-WME) method [37] and the ATC method[18]. The average root-mean-square error (ARMSE) is used to evaluate the accuracy of estimated results, which is defined as [33]:

$$\mathrm{ARMSE}=\frac{1}{U}\sum_{u=1}^{U}\sqrt{\frac{1}{M}\sum_{m=1}^{M}\left(\Delta\hat{\theta}_{u,m}-\Delta\theta_{u,m}\right)} \tag{47}$$

where $U$ denotes the number of experiments and $\Delta\hat{\theta}_{u,m}$ is the estimated phase error of the $m$-th channel in the $u$-th experiment.

The ARMSE versus SNR results are shown in Fig. 11. It can be seen that all three image-domain methods performs better than ATC method (green line). ISP method (red line) performs well for high SNRs. However, with the decrease of SNR, the estimation accuracy of ISP declines severely. This is because ISP is essentially a subspace method, and operated on focused SAR image data; the decomposition of signal subspace and noise subspace from image data is heavily influenced by noise level in the data. Moreover, in order to obtain the noise subspace, the ISP method requires at least one redundant channel, and as a result, it may fail in some special cases. Compared with ISP, the LML-WME method (blue line) is less affected by SNR. But its estimation accuracy is worse than ISP in high SNR case. Besides, the LML-WME method exploits coarsely focused image instead of well-focused image to estimate phase error, leading to degradation in its estimation accuracy to some extent. The proposed MNIS method (black line) is most stable among the four approaches. The level of its ARMSE is under 0.08 ° with SNR from 25dB to 0dB. Especially in low SNR case, it clearly outperforms both LML-WME and ISP methods.

TABLE II
SIMULATION PARAMETERS FOR A FIVE-CHANNEL SAR SYSTEM

| Parameter | Value |
|---|---|
| Carrier frequency | 9.6GHz |
| Platform velocity | 6811m/s |
| Slant range | 1050Km |
| Channel numbers | 5 |
| Displacement between adjacent channels | 3m |
| Doppler bandwidth | 2800Hz |
| Pulse repetition frequency | 800Hz |
| Signal bandwidth | 45MHz |

### B. *Experiment for Real SAR Data*

The real SAR data were acquired by a C-band airborne azimuth multi-channel SAR system whose parameters are shown in Table III. The system was operated in side-looking and strip-map mode. The Doppler bandwidth is about 950Hz and PRF is 385Hz. The azimuth spectrum ambiguity number is about 2.5 and the channel number is 4. In order to evaluate the channel phase error estimation performance better, the amplitude and time delay errors between channels are compensated in advance using methods introduced in Section III. The first channel is set as the reference channel. The estimated amplitude errors of these four channels are 1.0, 0.82, 0.89 and 0.91 respectively and the estimated time delay errors are 0ns, -0.16ns, -5.14ns and 0.47ns respectively.

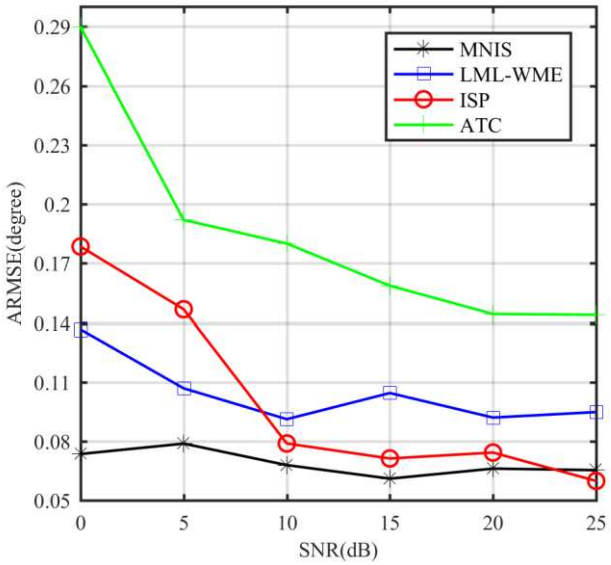


Fig. 11. ARMSE of estimated error versus SNR.

Fig. 12. shows the processing results of the four-channel data. The selected region contains sea and land with some strong targets. Fig. 12. (a) is the imaging result without channel phase error compensation, from which one can see that there exist obvious ghost targets. The real targets and ghost targets are marked with red rectangles separately. Fig. 12. (b) and (c) illustrate the imaging results by the LML-WME method and ISP method, respectively, in which ghost targets have almost disappeared. However, there are still some remains of the ghost targets which are visible after enlarging the region. The imaging result processed by the MNIS method is shown in Fig. 12. (d), where the ghost targets are suppressed significantly and they can hardly be seen in the enlarged image.

TABLE III
SYSTEM PARAMETERS FOR REAL MEASURED DATA

| Parameter | Value |
|---|---|
| Carrier frequency | 5.4GHz |
| Platform velocity | 118.434m/s |
| Channel numbers | 4 |
| Doppler bandwidth | 950Hz |
| Pulse repetition frequency | 385Hz |
| Signal bandwidth | 210MHz |
| Slant range | 9475m |

Since the azimuth spectrum ambiguity number is about 2.5, it is possible to use data of three channels to form a SAR image. In order to further verify the robustness of the method, data from three channels are processed by different approaches. Fig. 13. (b) and (c) shows the imaging results by the LML-WME and ISP methods. Although ghost targets are suppressed a lot compared with the uncompensated image in Fig. 13. (a), they are still visible. Fig. 13. (d) shows imaging result processed by the MNIS method. Obviously, the suppression of ghost targets in Fig. 13. (d) is much better than that in Fig. 13. (b) and (c).

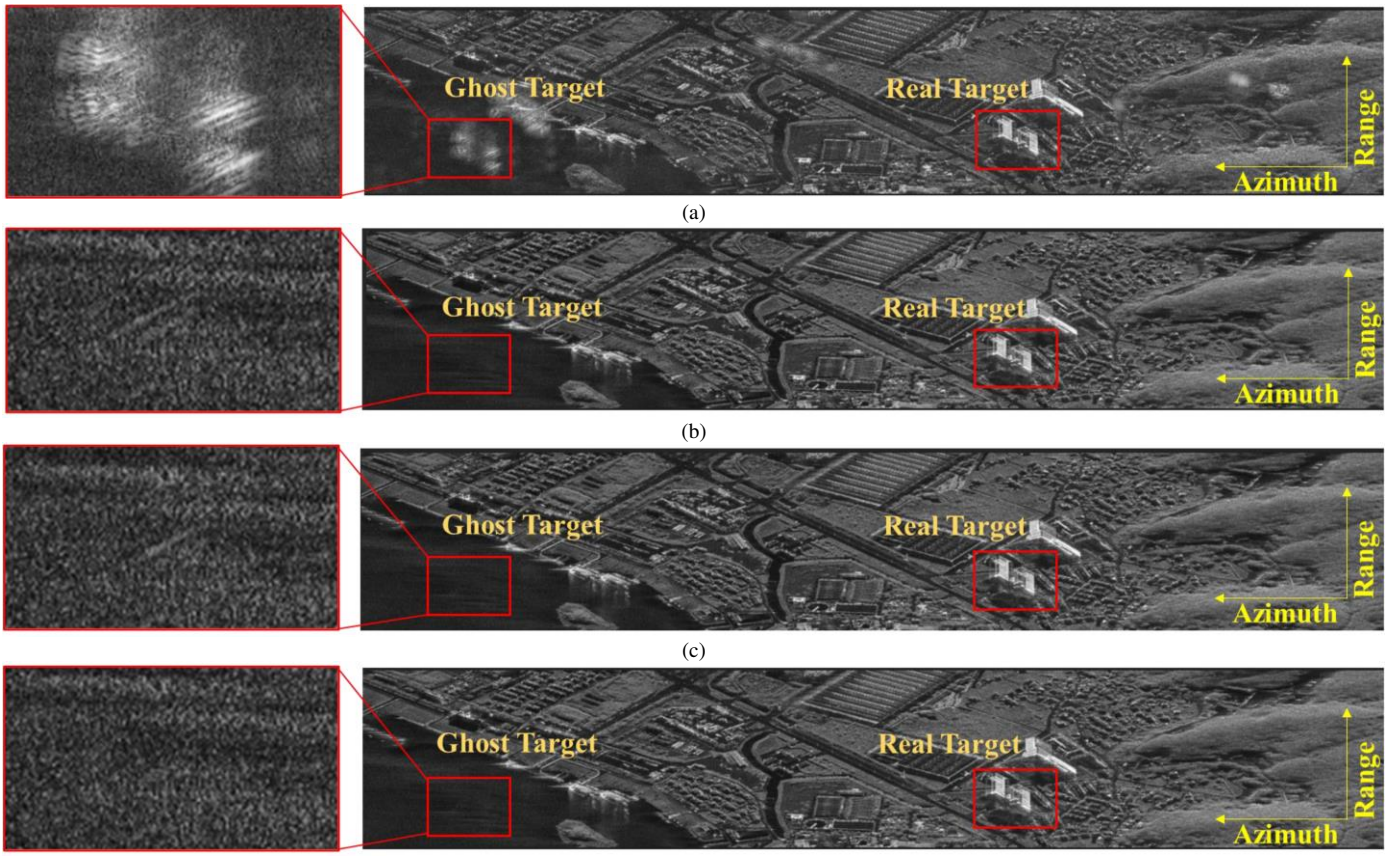


Fig. 12. Imaging results by different methods using data from four channels. (a) Imaging result without phase error correction. (b) Imaging result by the LML-WME method. (c) Imaging result by the ISP method. (d) Imaging result by the proposed method.

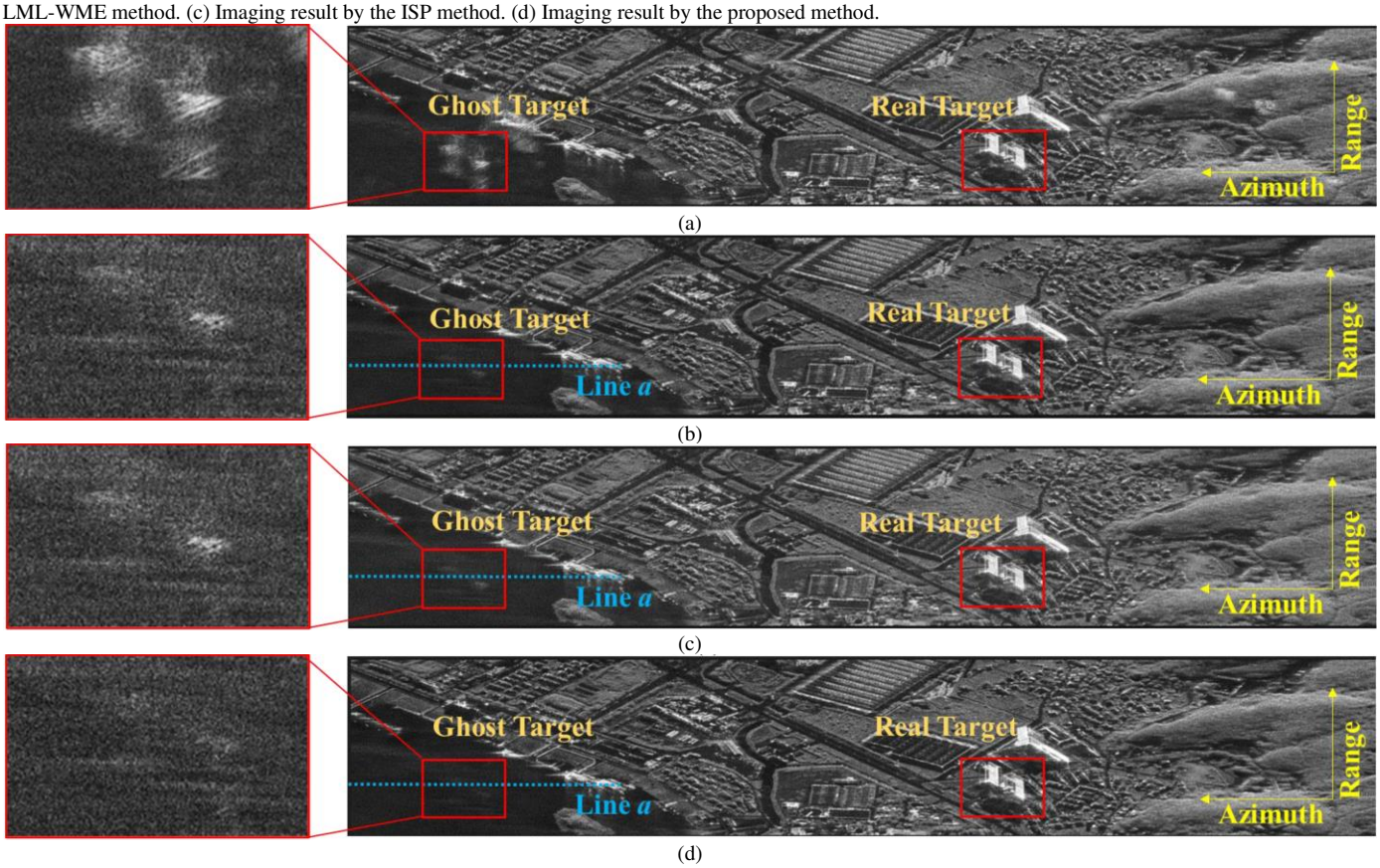


Fig. 13. Imaging results by different methods using data from three channels. (a) Imaging result without phase error correction. (b) Imaging result by the LML-WME method. (c) Imaging result by the ISP method. (d) Imaging result by the proposed method.

In order to better compare the degree of suppression for ghost targets, azimuth profiles of ghost target region along bule-dashed lines in Fig. 13 are extracted and shown in Fig. 14 (a). Fig. 14. (b) is the local enlargement result of ghost target region in Fig. 14. (a). It can be observed that the proposed MNIS method (green lines) has a better suppression for the ghost target than the ISP method (blue lines) and LML-WME method (red lines). There are mainly two reasons:1) As the channel number is close to the ambiguity number, it is difficult to achieve noise subspace decomposition from the cross-correlation matrix, which degrades the performance of the ISP method; 2) Reduction of channel number decreases SNR of the focused image. Compared with the MNIS method, ISP and LML-WME are more sensitive to image SNR. As a result, estimation accuracy of these two methods falls while the proposed MNIS method still maintains a good performance in this case.

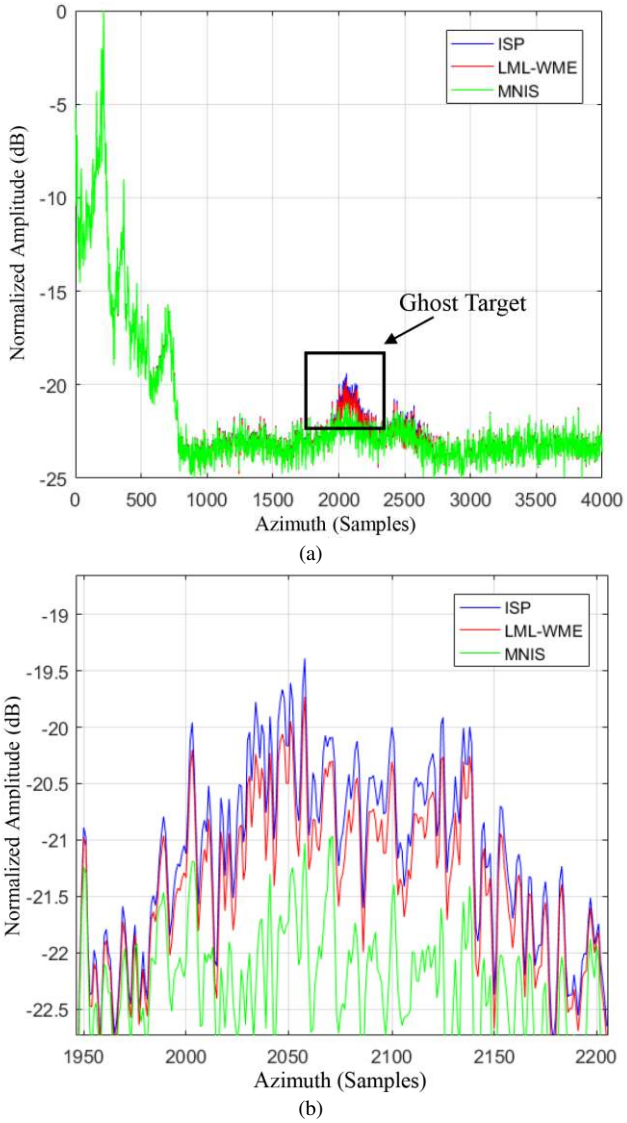


Fig. 14. Azimuth profiles of ghost target region with different methods. (a) Azimuth profiles along blue-dashed lines in Fig. 13. after normalization. (b) Local enlargement result of ghost target region in Fig. 14. (a).

To quantitatively analyze the effectiveness of different methods, the ghost-real target energy ratio (GTER) is employed to measure the suppression of ghost target in the final focused image, which is defined as:

$$\mathrm{GTER} = 20\log_{10}\frac{\max(|\mathrm{I_G}|)}{\max(|\mathrm{I_R}|)} \tag{48}$$

where $\max(|\mathrm{I_G}|)$ denotes the maximum amplitude value of pixels of ghost targets and $\max(|\mathrm{I_R}|)$ denotes the maximum value of pixels of real targets. The more accurately phase errors are compensated, the smaller GTER is. Generally, it is difficult to measure the amplitude of ghost targets when they are covered by clutter or strong targets. Fortunately, some ghost targets are located on sea in the processed image, making it possible to evaluate ghost targets' intensity. The regions marked with red rectangles in Fig. 12. and Fig. 13. are selected to measure GTER. The measured results of different images calibrated by different methods are listed in Table IV. When the processed channel number is four, GTER of the MNIS method is about 0.05dB better than the other two methods. When the processed channel number is three, GTER of the MNIS method is about 2dB better than ISP and LML-WME.

The computational efficiency of the ISP method, the LML-WME method, and the proposed method is also compared. The ISP method does not need iteration and has the lowest computational load. However, it suffers from performance degradation when there is no redundant channel, which limits the application of this method. The proposed MNIS method and LML-WME method both require iteration. Their complexity is determined by the number of iterations and computational load of each iteration step. The MNIS method estimates channel phase errors by BFGS-based quasi-Newton algorithm, which is a second order convergence optimizing algorithm. While the LML-WME method employs coordinate descent algorithm, in which only one parameter is updated at a time. Consequently, the proposed method has a higher convergent speed and less computational load than LML-WME method. The time consumed by different algorithms are recorded in Table IV. For the MNIS and LML-WME method, the same termination condition is set. The results show that the proposed method could greatly reduce execution time compared with LML-WME method while maintain high estimation accuracy.

TABLE IV
GTER OF DIFFERENT METHODS

| Number of Processed Channels | Method | GTER | Execution Time |
|---|---|---|---|
| 4 | Without Compensation | -43.71dB | \ |
| | LML-WME[37] | -51.61dB | 14.3s |
| | ISP[36] | -51.63dB | 1.5s |
| | MNIS | -51.68dB | 6.3s |
| 3 | Without Compensation | -34.96dB | \ |
| | LML-WME[37] | -44.66dB | 5.5s |
| | ISP[36] | -44.15dB | 1.2s |
| | MNIS | -46.47dB | 3.4s |

Fig. 15. illustrates the NIS after each iteration with different initial values when estimating phase errors via the proposed method. When coarsely estimated phase errors are set as initial values, a satisfactory result can be achieved after about 3 to 4 iterations. However, at least 6 iterations are required to get the same estimation accuracy with zero as initial values. This shows the fast convergence of the proposed method. By setting initial values properly, sufficiently accurate estimation result can be obtained quickly after only a few iterations based on the BFGS algorithm.

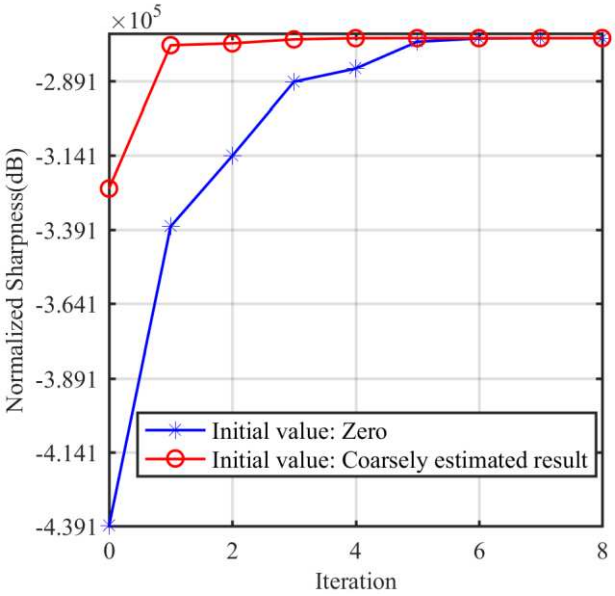


Fig. 15. Normalized image sharpness after each iteration.

### C. *Experiment for Range-variant Phase Error Compensation*

To demonstrate the effectiveness of the range-variant phase error compensation scheme, data with a wider swath are processed. After amplitude and time delay error correction, images of each channel are obtained by azimuth spectrum recovery and imaging processing. Next, images are divided into eight blocks along range. In each block, the MNIS method is used to estimate phase errors. The range-variant phase errors are then acquired by weighted least squares estimation, which are shown in Fig. 16. The first channel is set as the reference channel. In Fig. 16, discrete points represent estimated phase errors of different blocks, while lines are weighted least squares estimation results. According to equation (5), antenna position errors will cause range-varying phase errors. As antenna position errors are usually different for each channel, the slopes of phase error for each channel may also be different. As shown in Fig. 16., the variation of phase errors is up to almost 100 degrees for the fourth channel, meaning that the range-variance of phase error cannot be ignored when processing wide-swath data. The final well-calibrated image is shown in Fig. 17. (b). Compared with the uncompensated image in Fig. 17. (a), ghost targets in the whole image region are suppressed effectively after range-variant phase error correction as shown in Fig. 17. (b).

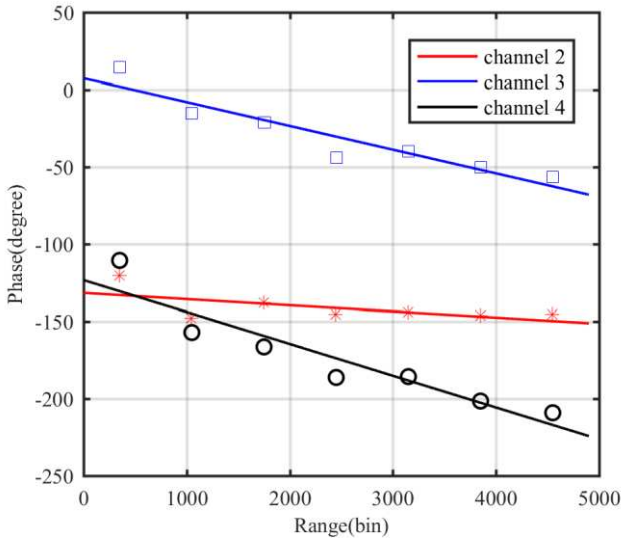


Fig. 16. Estimated range-variant phase errors of different channels.

## VII. Conclusion

In this article, a novel channel inconsistency error estimation method for azimuth multi-channel HRWS SAR system has been proposed, consisting of three steps: coarse channel mismatch compensation, azimuth spectrum recovery and image formation for each channel, range-variant channel phase error estimation and correction via the proposed MNIS method. In order to better evaluate the influence of channel phase errors on the SAR image, NIS is utilized as a criterion to assess the SAR image quality. Analysis and experiments show that NIS reaches maximum value when phase errors are compensated accurately. As this criterion can evaluate the suppression of ghost targets as well as the degree of focus of real targets, the proposed MNIS method is capable of maintaining a high estimation accuracy when ghost targets are not visible in some special cases, such as low SNR or strong clutter. A mathematical model is established between channel phase errors and NIS. Phase error estimation is transformed into an image quality optimization problem. By deriving the objective function gradient, channel phase errors are obtained by BFGS-based quasi-Newton method. The range-variance of channel phase errors is also considered by dividing images into different blocks along range direction. The performance of the proposed method is validated by both simulated data and real airborne multi-channel SAR data in comparison with other methods. Results show that the proposed approach can estimate channel phase errors more accurately and robustly by optimizing the final SAR image quality.

(a)

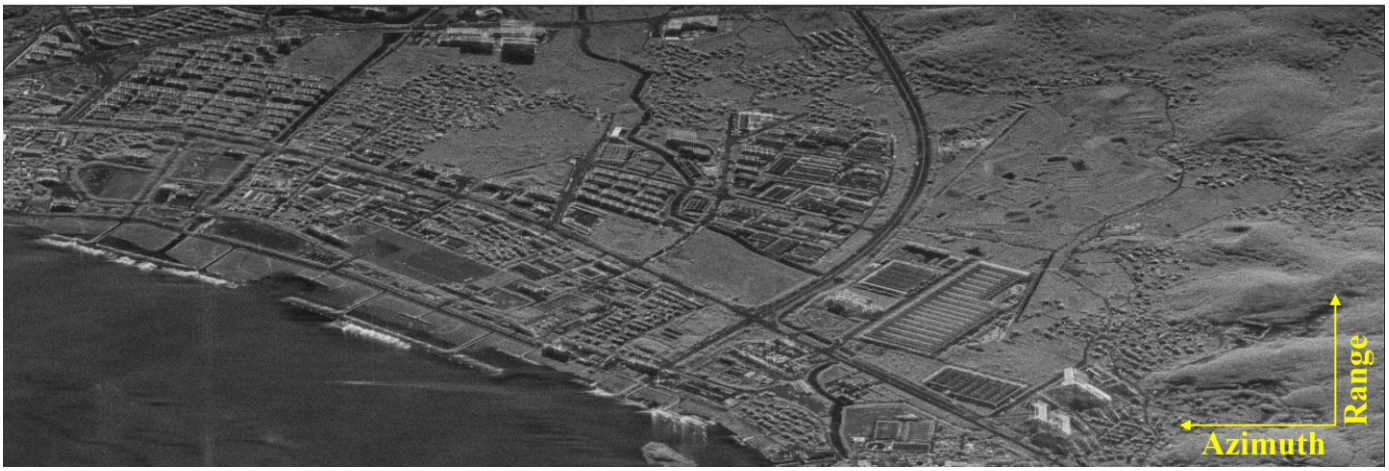


(b)

Fig. 17. (a) Imaging result without phase error compensation (b) Imaging result after range-variant phase error compensation.

## APPENDIX A

Consider a scatter point in a multi-channel SAR image. Assume energy of this scatter point without channel inconsistency error is $A$. When there are channel phase errors, ghost targets will appear symmetrically on both sides of this point target along azimuth direction. The energy of the scatter point and its ghost targets are expressed as:

$$B_i \quad i=-M,...,M \tag{A1}$$

in which $B_0$ is the energy of real target and $B_i \quad i=\pm1,\pm2,...,\pm M$ denote energy of all ghost targets. After normalization, we have:

$$A=\sum_{i=-M}^{i=M} B_i \qquad A>0,\quad B_i>0 \tag{A2}$$

It is obvious that:

$$\begin{aligned}\ln(1+A)-\sum_{i=-M}^{M}\ln(1+B_i)&=\ln\left(\frac{1+A}{\prod_{i=-M}^{M}(1+B_i)}\right)=\ln\left(\frac{1+A}{1+\sum_{i=-M}^{M}B_i+C}\right)\\&=\ln\left(\frac{1+A}{1+A+C}\right)<0\end{aligned} \tag{A3}$$

in which $C$ is a positive constant. Since $\ln(1+A)>0$ and $\sum_{i=-M}^{M}\ln(1+B_i)>0$, we have:

$$-\ln(1+A)>-\sum_{i=-M}^{M}\ln(1+B_i) \tag{A4}$$

Equation (A4) means that the existence of ghost targets reduces normalized image sharpness. Therefore, NIS will reach its maximum value when all ghost targets are suppressed completely.

## APPENDIX B

The objective function can be written as:

$$J(\boldsymbol{\theta})=\sum_{n=1}^{N}\sum_{k=1}^{K}\left[-\ln\left(T^2+1\right)\right] \tag{B1}$$

in which

$$T=D\sqrt{\frac{NK}{\sum_{n=1}^{N}\sum_{k=1}^{K}|D|^2}} \tag{B2}$$

$$D=\sum_{m=1}^{M}\exp(j\theta_m)I_m(n,k) \tag{B3}$$

Firstly, the partial derivative of an arbitrary variable can be expressed as:

$$\frac{\partial J(\boldsymbol{\theta})}{\partial \theta_m} = -\sum_{n=1}^{N}\sum_{k=1}^{K}\left[\frac{1}{T^2+1}\cdot\left(\frac{\partial T^2}{\partial \theta_m}\right)\right] \tag{B4}$$

The partial derivative of $T^2$ is:

$$\frac{\partial T^2}{\partial \theta_m} = \left(\frac{NK\cdot\dfrac{\partial D^2}{\theta_m} - T^2\sum_{n=1}^{N}\sum_{k=1}^{K}\left[\dfrac{\partial D^2}{\theta_m}\right]}{\sum_{n=1}^{N}\sum_{k=1}^{K}\left[D^2\right]}\right) \tag{B5}$$

The partial derivative of $D^2$ is:

$$\frac{\partial D^2}{\partial \theta_m} = -2\,\mathrm{Im}\left(\exp(j\theta_m) I_m(n,k) D^*\right) \tag{B6}$$

Then, the gradient of objective function $J(\boldsymbol{\theta})$ can be obtained as:

$$\begin{aligned}\frac{\partial J(\boldsymbol{\theta})}{\partial \theta_m} = {} & 2\sum_{n=1}^{N}\sum_{k=1}^{K}\left[\frac{\mathrm{Im}\left(\exp(j\theta_m) T_m T^*\right)}{\left(T^2+1\right)}\right] \\ & -\frac{2}{NK}\sum_{n=1}^{N}\sum_{k=1}^{K}\left[\mathrm{Im}\left(\exp(j\theta_m) T_m T^*\right)\right]\cdot\sum_{n=1}^{N}\sum_{k=1}^{K}\left[\frac{T^2}{\left(T^2+1\right)}\right]\end{aligned} \tag{B7}$$

in which $T_m = I_m(n,k)\sqrt{\dfrac{NK}{\sum_{n=1}^{N}\sum_{k=1}^{K}|D|^2}}$, and $\mathrm{Im}(\cdot)$ denotes the imaginary component.

## REFERENCES


[1] A. Moreira, P. Prats-Iraola, M. Younis, G. Krieger, I. Hajnsek, and K. P. Papathanassiou, "A tutorial on synthetic aperture radar," *IEEE Geosci. Remote Sens. Mag.*, vol. 1, no. 1, pp. 6–43, Apr. 2013.

[2] Y. Wang, Z. Ding, P. Xu, K. Chen, T. Zeng and T. Long, "Strip Layering Diagram-Based Optimum Continuously Varying Pulse Interval Sequence Design for Extremely High-Resolution Spaceborne Sliding Spotlight SAR," *IEEE Trans. Geosci. Remote Sens.*, vol. 59, no. 8, pp. 6751-6770, Aug. 2021.

[3] G. D. Callaghan and I. D. Longstaff, "Wide-swath space-borne SAR using a quad-element array," *IEE Proc. —Radar, Sonar, Navigat.*, vol. 146, no. 3, pp. 159–165, Jun. 1999.

[4] M. Suess, B. Grafmueller, and R. Zahn, "A novel high resolution, wide swath SAR system," in *Proc. IEEE Int. Geosci. Remote Sens. Symp.*, Sydney, NSW, Australia, 2001, pp. 1013–1015.

[5] G. Krieger, N. Gebert, and A. Moreira, "Multidimensional waveform encoding: A new digital beamforming technique for synthetic aperture radar remote sensing," *IEEE Trans. Geosci. Remote Sens.*, vol. 46, no. 1, pp. 31–46, Jan. 2008.

[6] G. Krieger, N. Gebert, and A. Moreira, "Unambiguous SAR signal reconstruction from nonuniform displaced phase center sampling," *IEEE Geosci. Remote Sens. Lett.*, vol. 1, no. 4, pp. 260–264, Oct. 2004.

[7] G. Krieger, N. Gebert, and A. Moreira, "SAR signal reconstruction from non-uniform displaced phase centre sampling," in *Proc. IEEE Int. Geosci. Remote Sens. Symp.*, 2004, vol. 3, pp. 1763–1766.

[8] L. Brule, D. Delisle, H. Baeggli and J. Graham, "RADARSAT-2 Program update," *Proceedings. 2005 IEEE International Geoscience and Remote Sensing Symposium, 2005. IGARSS* '05., 2005, pp. 3.

[9] Y. Kankaku, S. Suzuki and Y. Osawa, "ALOS-2 mission and development status," *2013 IEEE International Geoscience and Remote Sensing Symposium - IGARSS*, 2013, pp. 2396-2399.

[10] J. Janoth, S. Gantert, T. Schrage and A. Kaptein, "Terrasar next generation - Mission capabilities," *2013 IEEE International Geoscience and Remote Sensing Symposium - IGARSS*, 2013, pp. 2297-2300.

[11] S. Huber et al., "Tandem-L: Design Concepts for a Next-Generation Spaceborne SAR System," *Proceedings of EUSAR 2016: 11th European Conference on Synthetic Aperture Radar*, 2016, pp. 1-5.

[12] M. Shang et al., "The Space-Time Variation of Phase Imbalance for GF-3 Azimuth Multichannel Mode," *in IEEE Journal of Selected Topics in Applied Earth Observations and Remote Sensing*, vol. 13, pp. 4774-4788, 2020.

[13] Zhenfang Li, Zheng Bao, Hongyang Wang and Guisheng Liao, "Performance improvement for constellation SAR using signal processing techniques," *in IEEE Transactions on Aerospace and Electronic Systems*, vol. 42, no. 2, pp. 436-452, April 2006.

[14] N. Gebert, F. Queiroz de Almeida and G. Krieger, "Airborne Demonstration of Multichannel SAR Imaging," *IEEE Geosci. Remote Sens. Lett.*, vol. 8, no. 5, pp. 963-967, Sept. 2011.

[15] I. Sikaneta and D. Cerutti-Maori, "Demonstrations of HRWS and GMTI with RADARSAT-2," *EUSAR 2012; 9th European Conference on Synthetic Aperture Radar*, 2012, pp. 263-266.

[16] J. Kim, M. Younis, P. Prats-Iraola, M. Gabele and G. Krieger, "First Spaceborne Demonstration of Digital Beamforming for Azimuth Ambiguity Suppression," *IEEE Trans. Geosci. Remote Sens.*, vol. 51, no. 1, pp. 579-590, Jan. 2013.

[17] T. Yang, Z. Li, Y. Liu, and Z. Bao, "Channel error estimation methods for multichannel SAR systems in Azimuth," *IEEE Geosci. Remote Sens. Lett.*, vol. 10, no. 3, pp. 548–552, May 2013.

[18] J. Feng, C. Gao, Y. Zhang, and R. Wang, "Phase mismatch calibration of the multichannel SAR based on azimuth cross correlation," *IEEE Geosci. Remote Sens. Lett.*, vol. 10, no. 4, pp. 903–907, Jul. 2013.

[19] A. Liu, G. Liao, Q. Xu, and L. Ma, "An improved array-error estimation method for constellation SAR systems," *IEEE Geosci. Remote Sens. Lett.*, vol. 9, no. 1, pp. 90–94, Jan. 2012.

[20] Yan-Yang Liu, Z. Li, Zhi-Yong Suo and Z. Bao, "A novel channel phase bias estimation method for spaceborne along-track multi-channel HRWS SAR in time-domain," *IET International Radar Conference 2013*, 2013, pp. 1-4.

[21] C. Fang, Y. Liu, Z. Suo, Z. Li and J. Chen, "Improved channel mismatch estimation for multi-channel HRWS SAR based on azimuth cross correlation," *Electronics Letters*, vol. 54, no. 4, pp. 235-237, Feb. 2017.

[22] Y. Liu, Z. Li, Z. Wang, and Z. Bao, "On the baseband Doppler centroid estimation for multichannel HRWS SAR imaging," *IEEE Geosci. Remote Sens. Lett.*, vol. 11, no. 12, pp. 2050–2054, Dec. 2014.

[23] T. Yang, Z. Li, Y. Liu, Z. Suo and Z. Bao, "Channel error estimation methods for multi-channel HRWS SAR systems," *2013 IEEE International Geoscience and Remote Sensing Symposium - IGARSS*, 2013, pp. 4507-4510.

[24] J. Guo, J. Chen, H. Zeng and W. Yang, "Scene Adaptive Phase Inconsistency Estimation for Multi-channel ScanSAR System," *IEEE Geosci. Remote Sens. Lett.*, vol. 19, pp. 1-5, 2022, Art no. 4018205.

[25] A. Liu, G. Liao, L. Ma and Q. Xu, "An Array Error Estimation Method for Constellation SAR Systems," *IEEE Geosci. Remote Sens. Lett.*, vol. 7, no. 4, pp. 731-735, Oct. 2010.

[26] S. -X. Zhang et al., "Multichannel HRWS SAR Imaging Based on Range-Variant Channel Calibration and Multi-Doppler-Direction Restriction Ambiguity Suppression," *IEEE Trans. Geosci. Remote Sens.*, vol. 52, no. 7, pp. 4306-4327, July 2014.

[27] X. Guo, Y. Gao, K. Wang and X. Liu, "Improved Channel Error Calibration Algorithm for Azimuth Multichannel SAR Systems," *IEEE Geosci. Remote Sens. Lett.*, vol. 13, no. 7, pp. 1022-1026, July 2016.

[28] H. Gao, J. Chen, W. Liu, C. Li and W. Yang, "Phase Inconsistency Error Compensation for Multichannel Spaceborne SAR Based on the Rotation-Invariant Property," *IEEE Geosci. Remote Sens. Lett.*, vol. 18, no. 2, pp. 301-305, Feb. 2021.

[29] T. Jin, X. Qiu, D. Hu, C. Ding, (2016). "Channel Error Estimation Methods Comparison under Different Conditions for Multi-channel HRWS SAR systems", *Journal of Computer & Communications*, vol. 04, no. 3, pp. 88-94, March 2016.

[30] Y. Liu, Z. Li, T. Yang and Z. Bao, "An Adaptively Weighted Least Square Estimation Method of Channel Mismatches in Phase for Multichannel SAR Systems in Azimuth", *IEEE Geosci. Remote Sens. Lett.*, vol. 11, no. 2, pp. 439-443, Feb. 2014.

[31] Z. Wang, Y. Liu, Z. Li, G. Xu, J. Chen, "Phase bias estimation for multi-channel HRWS SAR based on doppler spectrum optimization", *Electronics Letters*, vol. 52, no. 21, pp. 1805-1807, Oct. 2016.

[32] H. Gao, J. Chen, S. Quegan, W. Yang, and C. Li, "Parameter estimation and error calibration for multi-channel beam-steering SAR systems," *Remote Sens.*, vol. 11, no. 12, p. 1415, Jun. 2019.

[33] L. Zhang, Y. Gao and X. Liu, "Robust Channel Phase Error Calibration Algorithm for Multichannel High-Resolution and Wide-Swath SAR Imaging," *IEEE Geosci. Remote Sens. Lett.*, vol. 14, no. 5, pp. 649-653, May 2017.

[34] H. Huang et al., "A Novel Channel Errors Calibration Algorithm for Multichannel High-Resolution and Wide-Swath SAR Imaging," *IEEE Trans. Geosci. Remote Sens.*, vol. 60, pp. 1-19, 2022, Art no. 5201619.

[35] J. Xiang et al., "A Robust Image-Domain Subspace-Based Channel Error Calibration and Postimaging Reconstruction Algorithm for Multiple Azimuth Channels SAR," *IEEE Trans. Geosci. Remote Sens.*, vol. 60, pp. 1-18, 2022, Art no. 5215818.
[36] G.-C. Sun et al., "A postmatched-filtering image-domain subspace method for channel mismatch estimation of multiple azimuth channels SAR," *IEEE Trans. Geosci. Remote Sens.*, vol. 60, pp. 1–14, 2022.
[37] S. Zhang, M. Xing, X. Xia, Y. Liu, R. Guo and Z. Bao, "A Robust Channel-Calibration Algorithm for Multi-Channel in Azimuth HRWS SAR Imaging Based on Local Maximum-Likelihood Weighted Minimum Entropy," *IEEE Transactions on Image Processing*, vol. 22, no. 12, pp. 5294-5305, Dec. 2013.
[38] D. Liang et al., "A channel calibration method based on weighted backprojection algorithm for multichannel SAR imaging," *IEEE Geosci. Remote Sens. Lett.*, vol. 16, no. 8, pp. 1254–1258, Aug. 2019.
[39] Y. Cai, Y. Deng, H. Zhang, R. Wang, Y. Wu and S. Cheng, "An Image-Domain Least L1-Norm Method for Channel Error Effect Analysis and Calibration of Azimuth Multi-Channel SAR," *IEEE Trans. Geosci. Remote Sens.*, vol. 60, pp. 1-14, 2022, Art no. 5222914.
[40] G. Farquharson, P. Lopez-Dekker and S. J. Frasier, "Contrast-Based Phase Calibration for Remote Sensing Systems With Digital Beamforming Antennas," *IEEE Trans. Geosci. Remote Sens.*, vol. 51, no. 3, pp. 1744-1754, March 2013.
[41] T. J. Schulz, "Optimal Sharpness Function for SAR Autofocus," *IEEE Signal Processing Letters*, vol. 14, no. 1, pp. 27-30, Jan. 2007.
[42] Q. He, X. Sun, Z. Yan, B. Li and K. Fu, "Multi-Object Tracking in Satellite Videos With Graph-Based Multitask Modeling," *IEEE Trans. Geosci. Remote Sens.*, vol. 60, pp. 1-13, 2022, Art no. 5619513.
[43] D. F. Shanno, "Conditioning of quasi-Newton methods for function minimization", *Math. Comput*., vol. 24, no. 111, pp. 647-656, Jul. 1970
[44] I. G. Cumming and F. H. Wong, *Digital Processing of Synthetic Aperture Radar Data*, vol. 1, no. 3. Norwood, MA, USA: Artech House, 2005, pp. 108–110.
[45] Wei Ye, Tat Soon Yeo and Zheng Bao, "Weighted least-squares estimation of phase errors for SAR/ISAR autofocus," *IEEE Trans. Geosci. Remote Sens.*, vol. 37, no. 5, pp. 2487-2494, Sept. 1999.

**Wei Yang** was born in 1983. He received the M.S. and Ph.D. degrees in signal and information processing from Beihang University (BUAA), Beijing, China, in 2008 and 2011, respectively.

From 2011 to 2013, he held a Postdoctoral position with the School of Electronics and Information Engineering, Beihang University. Since July 2013, he has been with the School of Electronics and Information Engineering, BUAA, as a Lecturer. From 2016 to 2017, he researched as a Visiting Researcher with the Department of Electronic and Electrical Engineering, University of Sheffield, Sheffield, U.K. Since 2018, he has been an Associate Professor with the School of Electronics and Information Engineering, BUAA. He has authored or coauthored more than 60 journal and conference publications. His research interests include moving target detection, high-resolution spaceborne SAR image formation, SAR image quality improvement, and 3-D imaging.

**Jiayi Guo** was born in 1996. She received her B.S. degree in information and communication engineering from Beihang University (BUAA), Beijing, China, in 2018, and she is now pursuing her Ph.D.degree in signal and information processing in School of Electronics and Information Engineering, Beihang University. Her research interests include multi-channel SAR imaging and moving target image formation.

**Jie Chen** (Senior Member, IEEE) was born in 1973. He received the B.S. and Ph.D. degrees in information and communication engineering from Beihang University, Beijing, China, in 1996 and 2002, respectively.

Since 2004, he has been an Associate Professor with the School of Electronics and Information Engineering, Beijing University. From 2009 to 2010, he was a Visiting Researcher with the School of Mathematics and Statistics, University of Sheffield, Sheffield, U.K., working on ionospheric effects on low-frequency space radars that measure forest biomass and ionospheric electron densities. Since July 2011, he has been a Professor with the School of Electronics and Information Engineering, Beihang University. His research interests include multimodal remote sensing data fusion, high-resolution spaceborne synthetic aperture radar (SAR) image formation and SAR image quality enhancement.

**Wei Liu** (Senior Member, IEEE) received the B.Sc. and L.L.B. degrees from Peking University, Beijing, China, in 1996 and 1997, respectively, the M.Phil. degree from The University of Hong Kong, Hong Kong, in 2001, and the Ph.D. degree from the School of Electronics and Computer Science, University of Southampton, Southampton, U.K., in 2003.

He held a postdoctoral position with the University of Southampton and later with the Department of Electrical and Electronic Engineering, Imperial College London, London, U.K. Since September 2005, he has been with the Department of Electronic and Electrical Engineering, The University of Sheffield, Sheffield, U.K., first as a Lecturer and then a Senior Lecturer. He has published about 350 journal articles and conference papers, five book chapters, and two research monographs titled *Wideband Beamforming: Concepts and Techniques* (John Wiley, March 2010) and *Low-Cost Smart Antennas* (Wiley-IEEE, March 2019). His research interests cover a wide range of topics in signal processing, with a focus on sensor array signal processing and its various applications, such as robotics and autonomous systems, human–computer interface, radar, sonar, satellite navigation, and wireless communications.

Dr. Liu is a member of the Digital Signal Processing Technical Committee of the IEEE Circuits and Systems Society (a Secretary since May 2020) and the Sensor Array and Multichannel Signal Processing Technical Committee of the

IEEE Signal Processing Society (the Chair since January 2021). He is an Editorial Board Member of the *Frontiers of Information Technology and Electronic Engineering* journal and the *Journal of The Franklin Institute*. He was an Associate Editor of *IEEE Transactions on Signal Processing* from 2015 to 2019 and *IEEE Access* from 2016 to 2021.

**DENG JiaDong** was born in 1995. He received the B.S. degree in Information and Computational Science from Beihang University, Beijing, China, in 2017, where he is currently pursuing the Ph.D. degree in signal and information processing. His research interests include spaceborne synthetic aperture radar (SAR) image formation for TOPS mode and sliding spotlight mode.

**Yamin Wang** received the M.S. and Ph.D. degrees in information and communication engineering Beihang University (previously known as Beijing University of Aeronautics and Astronautics (BUAA)), Beijing, China, in 2016 and 2022, respectively. She is currently a Postdoctoral Fellow with the School of Electronics and Information Engineering, BUAA. Her research interest includes synthetic aperture radar(SAR), video SAR, ground moving target indication(GMTI) and SAR signal processing.

**HongCheng Zeng** (Member, IEEE) was born in 1989. He received the Ph.D. degree in signal and information processing from Beihang University, Beijing, China, in 2016. From 2016 to 2019, he held a Postdoctoral Position with the School of Electronics and Information Engineering, Beihang University, where he has been an Assistant Professor since August 2019. From 2016 to 2017, he researched as a Visiting Researcher with the School of Mathematics and Statistics, University of Sheffield, Sheffield, U.K., from 2017 to 2018. Since 2022, he has been an Associate Professor with the School of Electronics and Information Engineering, Beihang University. He has authored or coauthored more than 30 journal and conference publications. His research interests include high-resolution spaceborne SAR image formation, passive radar signal processing, and moving target detection.